metals

MDPI

Article

Computational Thermochemistry for Modelling Oxidation During the Conveyance Tube Manufacturing Process

Megan Kendall [1,*], Mark Coleman [2], Hollie Cockings [3], Elizabeth Sackett [1], Chris Owen [4] and Michael Auinger [5]

[1] Department of Materials Science and Engineering, Swansea University, Swansea SA1 8EN, UK; e.sackett@swansea.ac.uk
[2] Oxford Instruments NanoAnalysis, Halifax Road, High Wycombe, Bucks HP12 3SE, UK; mark.coleman@oxinst.com
[3] Frazer-Nash Consultancy, Hill Park South, Springfield Drive, Leatherhead, Surrey KT22 7LH, UK; hollie.cockings@fnc.co.uk
[4] Tata Steel (Tubes), Corby NN17 5UA, UK
[5] WMG, University of Warwick, Coventry CV4 7AL, UK; m.auinger@warwick.ac.uk
* Correspondence: m.kendall.2134577@swansea.ac.uk

Abstract: Conveyance tube manufacturing via a hot-finished, welded route is an energy-intensive process which promotes rapid surface oxidation. During normalisation at approximately 950 °C to homogenise the post-weld microstructure, an oxide mill scale layer grows on tube outer surfaces. Following further thermomechanical processing, there is significant yield loss of up to 3% of total feedstock due to scale products, and surface degradation due to inconsistent scale delamination. Delaminated scale is also liable to contaminate and damage plant tooling. The computational thermochemistry software, Thermo-Calc 2023b, with its diffusion module, DICTRA, was explored for its potential to investigate oxidation kinetics on curved geometries representative of those in conveyance tube applications. A suitable model was developed using the Stefan problem, bespoke thermochemical databases, and a numerical solution to the diffusion equation. Oxide thickness predictions for representative curved surfaces revealed the significance of the radial term in the diffusion equation for tubes of less than a 200 mm inner radius. This critical value places the conveyance tubes' dimensions well within the range where the effects of a cylindrical coordinate system on oxidation, owing to continuous surface area changes and superimposed diffusion pathways, cannot be neglected if oxidation on curved surfaces is to be fully understood.

Keywords: oxidation; modelling; steel; diffusion; heat treatment

Citation: Kendall, M.; Coleman, M.; Cockings, H.; Sackett, E.; Owen, C.; Auinger, M. Computational Thermochemistry for Modelling Oxidation During the Conveyance Tube Manufacturing Process. *Metals* **2024**, *14*, 1402. https://doi.org/10.3390/met14121402

Academic Editors: Hong Xiao and Chao Yu

Received: 15 October 2024
Revised: 5 December 2024
Accepted: 6 December 2024
Published: 7 December 2024

1. Introduction

Low carbon steel thick-walled conveyance tubes are employed in wide-ranging building and industrial service applications, e.g., Heating, Ventilation and Air Conditioning (i.e., HVAC systems), and petrochemical transport, where high pressures, e.g., refrigeration, and temperatures, e.g., a steam system, are possible. The manufacturing process must be designed to achieve the material and mechanical properties necessary for these service conditions. In the UK alone, there are approximately 425,000 km of mains water infrastructure supplying domestic and commercial settings [1] and, according to the 2021 Census, approximately 1.1 million homes in Wales depend on a mains gas or oil supply for central heating [2]. Component damage and failure due to surface defects associated with phenomena such as oxidation could therefore have far-reaching social and economic consequences [3]. However, it is a challenge for plants to optimise their processes to maximise product quality, capacity, process flexibility, and cost effectiveness whilst high temperature oxidation on curved surfaces is still relatively poorly understood.

1.1. Conveyance Tube Manufacturing Process

Mild steel is delivered as a coil formed from a continuous cast billet. The steel sheet then passes through an accumulator series and is cold worked by forming rolls into the required hollow, cylindrical geometry. At this stage, the sheet still has a fine, homogenous microstructure, ensuring technical standard-defined mechanical properties. High frequency induction (HFI) welding is used to join the formed ends of the steel sheet creating a heat affected zone (HAZ) and some residual stresses. Therefore, the tube is subsequently heated to a temperature of over 950 °C for 2–4 min in a walking beam furnace, which restores the bulk to the desirable austenitic phase, before cooling in air. Tubes produced in this manner have several advantages over their cold-forged equivalents, including improved toughness, ductility, and pressure integrity, giving them an overall higher factor of safety. However, rapid growth of a multi-phase layer of dark-coloured, brittle iron oxide scale is also observed. Further thermomechanical processing (TMP) is used to produce a range of tube wall thicknesses and tube diameters, achieved by a multi-pass stretch reduction of 3–5% reduction per stand, with the greatest reduction occurring in the first few stands). The processing temperature is defined by achieving a balance between strain hardening and softening to minimise deformation-induced point and line defects (which are also defined by chemical composition, initial microstructure and deformation condition, deformation rate), and maintaining the material in the austenitic region. Typically, hydraulic descaling is applied in a post-normalisation, pre-reduction 'descaling box' for its combined benefits of reduced scale compaction and partial cooling to the ideal stretch reduction temperature of 850 °C. A summary of the manufacturing process is shown in Figure 1.

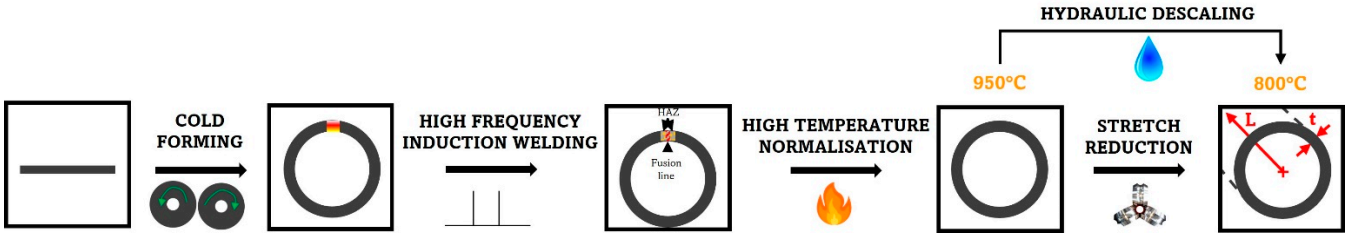

Figure 1. Schematic sequence of the conveyance tube manufacturing process.

Stretch reduction, and its associated high mechanical strain, causes the remaining scale to spall, leading to substrate exposure and surface wear. This has environmental and economic consequences as losses of up to 3% by weight occur due to scaling alone (equivalent to approximately 500 tonnes of feedstock loss per warehouse batch) [4]. There are also aesthetic implications due to either compaction of scale on the substrate surface ('rolled-in effect') and/or inadequate adherence of value-added coatings, e.g., anti-corrosion paint, and in-service surface performance problems. The resulting inconsistent scale adhesion that not only appears to give a poor surface finish but may also lead to complications for those customers who wish to apply additional paint or coat the tubes. Furthermore, scale removed either by descaling or spalling tends to disperse into the manufacturing environment, causing damage and contamination to product and plant alike.

1.2. Scale Management

Growth stress, arising from volumetric increase associated with oxygen uptake, depends on whether scale is internal or external and isotropic or radial, and is directly related to scale failure [5]. Matsuno et al. [6] specifically explored the impact of growth (oxidation) stress on descalability during a high-temperature hydraulic descaling operation. They also highlighted the Pilling and Bedworth ratio (PBR), which represents the ratio of oxide to metal volume as a measure of stress arising from volume dilatation during conversion of a metal to its oxide [7–9], which can be measured via deformation analysis. Ultimately, they proposed that oxidation stress is the dominant cause of adhesive failure within the combined effect of stress and adhesion vs. cohesion strength dominance, since temperature

will accelerate oxidation and cause great compressive volume dilatation. For austenitic steels, such as are seen during conveyance tube normalisation, the dominance of Cr^{3+} migration favours the development of external oxide, i.e., oxygen ions are diffusing as well as iron and chromium (III) for ferritic martensitic steels so they experience both external and internal oxidation [10]. Furthermore, assuming radial (anisotropic) oxide growth and absence of axial strain, growth stresses are a purely geometric, mono-axial effect only observed on curved surfaces (where planar surfaces have an infinite radius of curvature which drives quotient-based strain equations to 0) [11]. This supports Sabau and Wright's conclusions on the significant impact of geometry on spallation [12], thus showing that geometry has an impact on scale management practice. Scale can be managed via a reactive approach which aims to eliminate the problem after detection by identifying its root causes and amplifiers after repeated incidence. This can take the form of anti-oxidation coatings [13–15], the details of which are beyond the scope of this paper. However, a more proactive approach using modelling would allow the industry to account for scale kinetics phenomena during thermomechanical process design. Pillai et al. agreed in their review of models for oxidation-based high-temperature degradation that the mechanism and extent of high-temperature oxidation of low carbon steel is characterised as a function of alloy composition, temperature, time, growth kinetics, geometry, and service environment [16]. Computational process modelling, when optimally designed and validated, can identify routes to minimise costs, improve product quality, and increase output, based on an accurate and fast assessment of scale and its associated trends. There are several manufacturing benefits, including faster and cheaper product and process innovations, reduced downtime and maintenance, reduced material usage, and, overall, more robust processes. Furthermore, experimental validation of curved surface oxidation is challenging, particularly due to the limitations of equipment used in in situ oxidation investigations. Thermogravimetric furnaces, which provide continuous mass gain data, are often limited in their sample size capacity so only very small tubes can be used, or tubes have to be sectioned which causes machining-induced residual stress [17,18]. However, there are issues with TGA measurements, as they give the total oxidation on a sample and neglect the effect of the gas flow on the extent of oxidation in each part of the sample geometry, as shown in the work by Mori et al. [5]. Therefore, any experimental value derived from TGA curves is an average over the entire geometry which does not address the differences between the side facing towards the flow and the one facing away. This is a strength of modelling; its ability to distinguish between the two and the reason for focusing on the modelling studies and then subsequently correlate these with the total oxidation thickness measured after heat exposure (the latter being subject to errors due to spallation of poorly adherent oxides). Furnaces with a larger sample size capacity do not usually have TGA equipment so rely on pre- and post-heat treatment high resolution mass balance measurements of the sample. High temperature oxides are known to be brittle, as seen in observation by the authors and as reported by the literature [5,19–21]. This brittle nature makes scale spalling inevitable so that material is lost between transferring the sample from the furnace to a mass balance, in addition to losses during sample cooling before it is removed from the furnace due to thermal mismatch between the metal and oxide. Typical oxide thickness predictions can be derived from input of temperature-time profiles based on analytical or computational predictions of thermofluid phenomena. However, this method still requires considerable involvement via definition of any equations and models, and translation of their results into functions for parameters used to calculate rate constants such as in Sun et al.'s work [22]. CALPHAD-based ('Computer Coupling of Phase Diagrams and Thermochemistry') software can investigate the thermodynamics and material properties of an oxidising system via phase equilibria outputs. The CALPHAD methodology can obtain a feasibility description for alloy system reactions and their most likely phase product via the Second Law of Thermodynamics and a Gibbs Free Energy minimisation [23]. Such a system relies on a comprehensive thermodynamic database for all the elements concerned which undergoes assessment, model selection, optimisation, storage, and validation. As a

minimum, it must be possible to describe the enthalpy, entropy, and Gibbs' Free Energy of a solution (generally described using the sub-lattice modelling-based Compound Energy Formalism (CEF) for solid oxide systems) as a function of temperature and composition in order to perform accurate and versatile thermodynamic calculation [24]. Consequently, as with any computational model, descriptive accuracy must be balanced with mathematical feasibility based on the Central Processing Unit (CPU) resources available so that computation times are not excessive. However, ever-increasing computational power availability is accompanied by options for increasingly complex feasible models. Poerschke argues that understanding and prediction of spall-based surface degradation relies on an understanding of the 'interplay' between substrate and scale (as well as any applied coatings) and the thermodynamic information provided by computational materials engineering modelling when systems become complex, e.g., non-planar geometries [25]. The Thermo-Calc DICTRA commercial package has existed since 1994, but there have been few attempts to extend its application of the moving phase boundary approach beyond phase transformation applications [26]. Furthermore, where surface oxide layer growth has been explored using this software, the geometry has been limited to planar cases [3]. The use of DICTRA for surface oxide has also been inhibited by a lack of attempts to expand on existing commercial thermodynamic and mobility data sets to incorporate oxide phases.

1.3. Geometry Effects

Despite many experimental and computational investigations into oxidation kinetics and oxide adhesion during thermomechanical processes involving slab and/or strip steel [27–29], there is far less literature concerning oxidation phenomena on non-planar surfaces [11,12], such as those found in conveyance tube manufacturing. Works using a computational approach are rarer still and seldom focus on oxidation as the main phenomenon [30–32]. Nevertheless, investigations of wall temperature, reaction environment, and thermal stress are still valuable as precursory information for heavily temperature-dependent oxidation thermochemistry. Landfahrer et al. numerically modelled a full-scale reheating furnace for investigation of the effect of scale on heat transfer in low carbon steel tubes via extension of previous study [30]. The key advantage of their model was the coupling of two independent simulations (stationary combustion and single-tube transient heating) in place of a more computationally demanding fully transient, chemical kinetics analysis. However, even in these rare cases, existing works are dominated by studies of steam superheater systems where parallels can only be drawn to conveyance tube manufacturing in the case of 'fireside' corrosion of tubes within these systems. Equation (2) gives the diffusion equation in cylindrical coordinates, as is appropriate for conveyance tube geometry, where c_k is the species concentration as a function of time, t, and position, (r, ϕ, z). Dependency on the azimuthal, ϕ, and vertical, z, coordinates is eliminated by assuming rotational symmetry during oxidation, and changes in oxidation behaviour are only observed along the radial coordinate, r (see (2)).

$$\frac{\partial \mathrm{c_k}}{\partial \mathrm{t}} = \frac{1}{\mathrm{r}} \frac{\partial}{\partial \mathrm{r}} \left(\mathrm{r} \frac{\partial \mathrm{c_k}}{\partial \mathrm{r}} \right) + \frac{1}{\mathrm{r}^2} \frac{\partial^2 \mathrm{c_k}}{\partial \theta^2} + \frac{\partial^2 \mathrm{c_k}}{\partial z^2} \tag{1}$$

$$\frac{\partial c_k}{\partial t} = D \left(\frac{1}{r} \frac{\partial c_k}{\partial r} + \frac{\partial^2 c_k}{\partial r^2} \right) \tag{2}$$

Changes in radius are accompanied by a change in available reacting surface area and surface area to volume ratio (see Figure 2), and highlight how an increase in radius is accompanied by an increase in surface area, A, (see (3)) and a decrease in surface area to volume ratio, $A : V$ (see (4)). Therefore, the surface area increases during inner surface oxidation (consumption of the substrate widens the cylinder bore, i.e., the inner radius)

lead to an overall slower rate of reaction and therefore thinner oxide thickness after a given time and, as such, the converse is true of the outer surface.

$$A = 2\pi r_{3_{t=t}} z \tag{3}$$

$$A : V = \frac{2r_{3_{t=t}}}{{r_{3_{t=t}}}^2 - {r_{2_{t=t}}}^2} \tag{4}$$

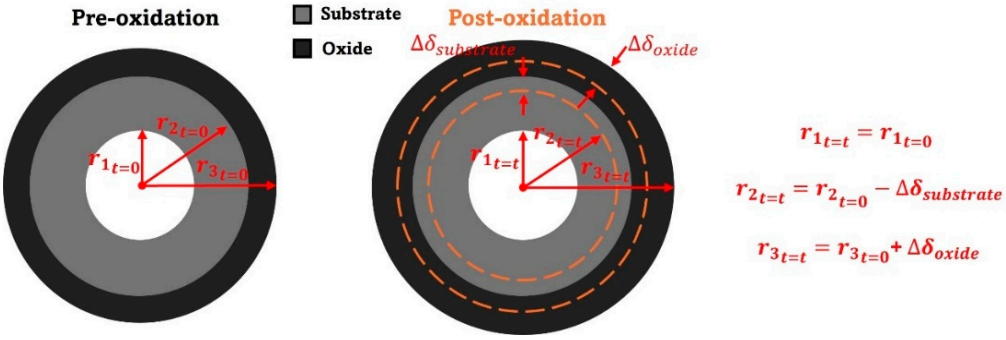

Figure 2. Diagram showing changes in cylinder outer radius during surface oxidation both pre- and post-oxidation (adapted from source [33]).

1.4. Oxidation Theory for a Computational Approach

Low carbon steel oxidation kinetics are defined by either a linear or parabolic rate law (dependent on instantaneous oxidation time and temperature considered) [34]. As most steel reheat treatments are long, high-temperature processes, including tube normalisation, a logarithmic rate law description is not appropriate. Initially, external oxidation of steel is governed by phase boundary processes at the substrate–scale (SSI) and scale–gas (SGI) interfaces. For the SGI, the rate of mass transport of oxygen-containing gas to the surface for adsorption, splitting to free oxygen, chemisorption, lattice incorporation, nucleation, and growth, is the most critical interface phenomenon and governs the linear rate law, i.e., it is assumed that, initially, kinetics are dominated by gas transport from the environment to the interface [35]. However, during the later stages of oxidation, kinetics are dominated by ion diffusion phenomena in the oxide. To maintain equilibrium and high metal activity as oxidation proceeds, there must be electron mobility, and ion flux levels must be maintained as the flux path lengthens due to scale thickening. Surface reaction rate, i.e., SGI activity, must fall to satisfy this constraint via a reduction in iron ion diffusion, making it the rate-controlling step. This kinetic change triggers a transition from a linear to parabolic rate law profile. Hence, kinetics are controlled by the dynamic balance of oxygen adsorption and iron ion diffusion during scale thickening and established oxidation is characterised by diffusion. Iordanova et al. argue that the strong influence of ion diffusion phenomena on oxidation further supports the assumption of a parabolic rate law for high-temperature investigations [34]. The relative thicknesses of the three phases (wustite, magnetite, and haematite in a 95:4:1 ratio) typically present on heat-treated low carbon steel also reflect this assumption of bulk diffusion-controlled (i.e., parabolic) oxidation and local thermodynamic equilibrium at phase interfaces, as wustite has a much greater iron diffusion coefficient than magnetite and haematite [36]. Highly defective crystal lattices, generated by divalent and trivalent interstitial iron cations, are the source of both outward cation and inward anion diffusion. Vacancies allow ions to 'jump' and thus move through the crystal lattice unimpeded, provided enough energy is supplied. Modelling of this process demands an understanding of the concept of sublattices, which are either tetrahedral or octahedral in the Fe-O system. Scale formed on grades similar to those used in tube manufacturing is dominated by wustite, a non-stoichiometric halitic phase $Fe_{1-x}O$ [37]. Hidayat et al. argued that there is insufficient reliable quantitative data on sublattice site occupancy, defect composition, and defect clustering to develop a comprehensive thermodynamic

model of the halitic wustite structure (ideal, stoichiometric, or otherwise) [38]. Nevertheless, such a model is required to generate comprehensive analytical and computational models, and they therefore accept the assumption made by Sundman et al. that iron cations and vacancies can only mix on octahedral sublattice sites, i.e., iron cations present on tetrahedral sites are ignored. The resulting simplified sublattice formalism for wustite is given below [39].

$$\left(Fe^{+2}, Fe^{+3}, Va\right)_1\left(O^{-2}\right)_1$$

Hallstrom et al. asserted that diffusion of Fe can be modelled without consideration of its valency as crystal lattice electrons are significantly more mobile in wustite than Fe cations at high temperatures (T > 600 °C) [40]. The formula unit can therefore be simplified as below,

$$(Fe, Va)_1(O)_1$$

which provides the necessary information to analytically define the system, specifically the flux, J, and bulk chemical diffusion coefficient, D, of both the iron and oxygen species. Without a driving force, the energy barrier to diffusion (specifically that required to allow an atom to jump to an empty lattice site) is defined by the free energy of migration, G_m. (Then 5 shows how diffusivity is defined in part by atomic mobility, M, due to continuous random movement in the absence of a driving force in this case (where R and T are the molar gas constant (8.31 $J{\cdot}K^{-1}{\cdot}mol^{-1}$) and temperature (K), respectively).

$$D = RTM \tag{5}$$

Hallstrom et al. [3] used Thermo-Calc's Diffusion Module ('DICTRA') to numerically solve the 1D diffusion equation, i.e., for a planar geometry, and computationally predict oxidation kinetics. Xia et al. argue that the use of a 1D system ignores the realistic 2D composition distribution of the material and restricts diffusion coefficient calculations to fixed compositions or those that only vary compositionally in a single direction [41]. When diffusion across a non-planar boundary, such as is found on a curved surface, is under investigation, the computational domain must be complexified to accurately account for two dimensions. Since both species flux and temporal concentration gradient, $\frac{\partial c_k}{\partial t}$, are unknown variables, the equation for mass conservation in the absence of chemical reactions must be coupled to Fick's First Law, which relates flux and spatial concentration gradient, $\frac{\partial c_k}{\partial z}$, via a chemical diffusion coefficient, to derive Fick's Second Law (see (6)).

$$\frac{\partial c_k}{\partial t} = D\frac{\partial^2 c_k}{\partial z^2} \tag{6}$$

Computational solutions for the independent flux of metal cations and oxygen anions for the two phases can be supplied to Fick's Second Law, alongside volume and molar fractions which are defined experimentally (via advanced imaging techniques) and computationally (via phase diagram simulations), respectively. A moving phase boundary ('Stefan problem') formulation for diffusion is used and the output of (6) is a description of the migration rate of the boundary between two phases, i.e., metal and oxide, when the flux of species k out of one phase, α, and into another, β, respectively, is not balanced, i.e., $J_k^{\alpha} - J_k^{\gamma} \neq 0$ [42]. The presence of the moving boundary renders this problem non-linear, combining PDEs and complicated interphase geometrical movement, and it is difficult to obtain analytical solutions without oversimplification. The moving phase boundary approach is most suitable for isobarothermal binary systems where the interfacial compositions are fixed so the numerical efficiency of the approach can be maintained [43]. Thus, oxide thickness, $\Delta\delta_{t_{step}}$, after a given timestep, t_{step}, can be predicted using (7), and the cumulation of values from each timestep shows the time-dependent kinetic trends (for a given temperature).

$$\Delta\delta_{t_{step}} = V_m^{\alpha} \frac{J_k^{\alpha} - J_k^{\gamma}}{x_k^{\alpha} - x_k^{\gamma}} t_{step} \quad (7)$$

As previously mentioned, diffusion in interstitial alloys with small migrating interstitials, e.g., oxygen in iron, in dynamic equilibrium with each other is characterised by a continual vacancy migration mechanism. In (5), the authors show that the variables for a successful computation of diffusion depends on accurate expressions for the bulk mobility of all involved species. The species molar fraction to substitutional element (oxygen) contribution, u_k, and chemical potential derivative, $\frac{\partial \mu_k}{\partial u_k}$, are derived from the literature. Application of (7) relies on an assumption of a planar diffusion front (long diffusion period and small grains) to ensure diffusion field overlap around neighbouring grain boundaries. This can be reasonably assumed in compounds such as wustite where the grains are small compared to the oxide scale thickness and therefore the metal–oxide interface is straight at the relevant length scales [3]. The final key assumption is that of an Arrhenius-type expression for bulk mobility, including a pre-exponential coefficient, M_0, and activation energy, Q (see (8)).

$$M_k = M_0 e^{-\frac{Q}{RT}} \quad (8)$$

It is noted that, alongside temperature, mobility is also influenced by oxygen partial pressure when considering oxide phases (unlike diffusion due to the strength of atomic binding) and the dopant effect of certain alloy elements. However, accounting for these effects is beyond the scope of this work. Overall, oxidation as a phenomenon is complex and dependent on multiple parameters. However, oxidation in the context of the tube production process is further complicated by manufacturing parameters and tube geometry. The increased computational resources available in the 21st century could be used to improve the depth and accuracy of knowledge surrounding scale kinetics, morphology, and adhesion on curved surfaces across a range of conditions not limited to the design envelope. The work within this paper aims to explore the potential for using a computational thermodynamics approach to understand scale kinetics phenomena during tube normalisation. In particular, the Stefan problem moving phase boundary methodology is applied to a new context, i.e., tube normalisation, so hollow cylindrical geometry and high temperature low carbon steel and scale phases and appropriate tube manufacturing-friendly thermodynamic and kinetic phase databases are developed. A high accuracy Simultaneous Thermal Analysis (STA) approach, comprising Thermogravimetric Analysis (TGA) and Differential Scanning Calorimetry (DSC) techniques, is used for validation to accelerate the analysis of tube oxidation under normalisation conditions.

2. Materials and Methods

2.1. Materials

The materials under investigation during in situ oxidation tests for validation purposes were the two grades of low carbon, low alloy steel P235GH and P265GH (compliant with the material specification BS EN10217-2 [44]). The specification given in BS EN10217-2 is outlined in Table 1. Nose crop samples of both grades were supplied by Tata Steel Tubes UK Ltd in Corby, UK.

Table 1. Alloy element composition limits specified by BS EN 10217-2 (welded steel tubes for pressure purposes—technical delivery conditions [part 2: electric welded non-alloy and alloy steel tubes with specified elevated temperature properties]) for steel grades P235GH and P265GH.

% by Mass of Element	C	Si (max.)	Mn	P (max.	S (max.)	Cr (max.)	Mo	Ni (max.)	Al (total)	Cu (max.)	Nb (max.)	Ti (max.)	V (max.)	Cr + Cu + Mo + Ni (max.)
P235GH	≤0.16	0.35	≤1.20	0.025	0.020	0.30	≤0.08	0.30	0.020	0.30	0.010	0.03	0.02	0.70
P265GH	≤0.20	0.40	≤1.40	0.025	0.020	0.30	≤0.08	0.30	0.020	0.30	0.010	0.03	0.02	0.70

2.2. Computational Methodology

Although sublattice models exist for all three oxide phases found on low carbon steel, for simplicity of the initial model pre-processing, the entire scale layer was assumed to be wustite. Field Emission Gun Scanning Electron Microscopy (FEGSEM) imaging, coupled with Energy Dispersive Spectroscopy (EDS) of the oxide on a normalised tube sample revealed a comparatively compact, homogeneous scale (see Figures 3–5).

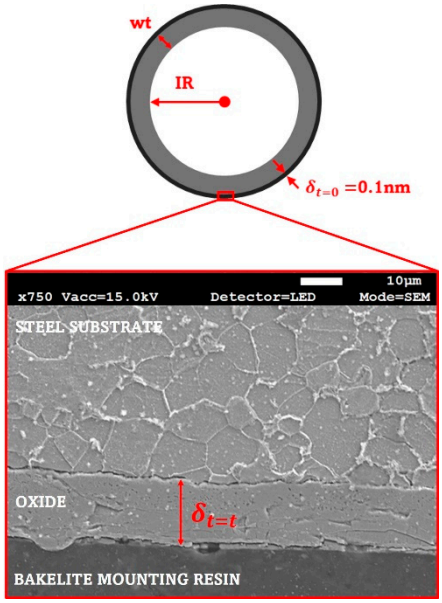

Figure 3. FEGSEM image of oxide found at the outer surface of the tube wall for sample with a 20.5 mm internal diameter.

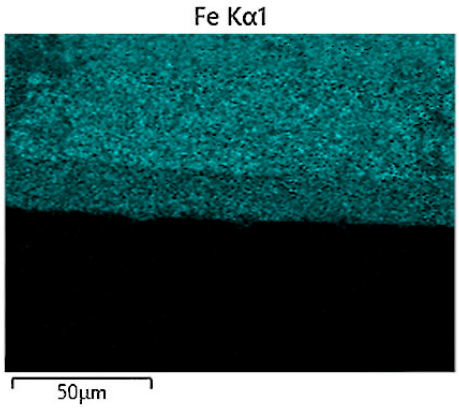

Figure 4. EDS map of iron (Fe) contribution for section of oxide formed on outer surface of a 15 nb tube sample post-normalisation in industry.

The Fe-O binary system phase diagram was used to determine the phases present and their relevant mole fractions at the normalisation temperature of 1223 K. Initial compositions of oxygen and iron were supplied as left and right interface boundary conditions for each region (austenite and wustite), respectively. Composition can only vary along one spatial coordinate, and only substitutional elements contribute to volume. For the overall system of finite volume cells, composition gradients are only considered between cells rather than inside. The metal and scale regions are joined by a finite interfacial region comprising two cells (one from each region). Local equilibrium is assumed to hold between the two regions, with constant volume fractions of each phase.

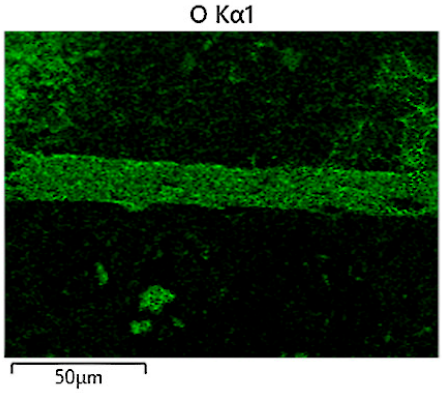

Figure 5. EDS map of oxygen (O) contribution for section of oxide formed on outer surface of a 15 nb tube sample post-normalisation in industry.

A cylindrical cross-sectional geometry of infinite length was used (see Figure 3). Inner radius and wall thickness were set at values associated with typical conveyance tube dimensions. Control of these two parameters makes the model well-suited to hot-finished conveyance tubes, which are manufactured with a controlled inner radius, IR, and a variable wall thickness, wt. The initial wustite thickness, $\delta_{t=0}$, was unchanged at 0.1 nm.

The inability to define the oxide region as halite (the most accurate microstructural representation of the wustite scale phase [39]) prevented the use of the commercial TCFE12 and MOBFE7 databases available in Thermo-Calc (although data for magnetite and haematite were used as part of the subsequent bespoke database development). Inspection of the phase and phase composition inventory within the system definer revealed that mobility data, necessary to define diffusion, was not available in the Thermo-Calc database for common oxide scale microstructures (halite, spinel, corundum, etc.).

Initial database set-up relies on the definition of constituent elements (Fe and O in this case, along with vacancy and electron additions) in terms of their Stable Element Reference (SER) state (298.15 K, 1 bar) and enthalpy and entropy of formation. Stoichiometric formulae are also needed for each species to include atomic and ionic states as well as compounds. Gibbs Free Energy functions must also be defined ready for minimisation, which is an essential part of computational thermodynamics. These functions (see (9)) were taken from Sundman [39] and Kowalski and Spencer's [45] works describing the Fe-O system.

$$G_{FeO} = -279318 + 252.848T - 46.12826Tln(T) - 0.0057402984T^2 \quad (9)$$

Overall, wustite can have complex physical properties due to its non-stoichiometry, variable site distribution of ferric iron, clustering of defects, long- and short-range ordering, and exsolution. The level of non-stoichiometry in iron oxides is controlled by the concentration of cation (metal) vacancies evolved during the diffusion-controlled oxidation process, and heavily influenced by temperature and partial pressure. However, Hazen and Jeanloz remarked that wustite thermal expansion is not significantly affected by stoichiometry [46]. Furthermore, deviation of stoichiometry in wustite only becomes significant at temperatures lower than 800 °C, i.e., below typical normalisation temperatures.

2.2.1. Mobility Database Definition

Elements, species, constituents, and phases in the kinetic database were defined identically to those in the thermodynamic database. Volume data took a standard value for all relevant volume-contributing substitutional phases (including oxygen gas) of 1×10^{-5} m^3mol^{-1}, as defined in the Thermo-Calc database management documentation [47]. Interstitial species (O, Fe^{2+}, Fe^{3+}) were assigned as zero-volume species. Data for the FCC_A1 (austenite) phase (iron and oxygen diffusivity as described for ferrite) came from [48,49] in a diffusivity form, as did that of halite (wustite) from the widely accepted work of Kofstad [50].

An implicit Euler method was used for time discretisation where the unknown, concentrations were defined by coupled sets of equations. The simulation length, 180 s, was defined by the mean of the heat treatment period range in the normalisation furnace. The initial and minimum acceptable timesteps were both set at 0.1 ms, respectively. A convergence study was performed to assess the maximum timestep which provided the optimal balance of accuracy and computational efficiency. Although the default maximum timestep value for Thermo-Calc is 10 s, the use of a multi-resolution mesh (geometric for the austenite region and double geometric for the wustite region), to reflect the steep gradients of ion concentrations due to fluxing at both the steel–scale and scale–gas interfaces, increases the computational demand. For example, using a linear and geometric mesh for the austenite and wustite regions, respectively, led to a CPU demand of 77 s to solve for 204 datapoints. However, using the more appropriate geometric-double geometric approach (see Figure 6), making both the steel–scale and scale–gas interfaces regions of interest with the most elements, demanded 259 s to solve 324 datapoints. For timesteps greater than 10 s, there was a negligible change in CPU demand and a consistent < 1% decrease in maximum predicted oxide thickness. A maximum allowable timestep of 10 s (~3% of the total simulation test time) was therefore selected as the best balance of accuracy and CPU demands.

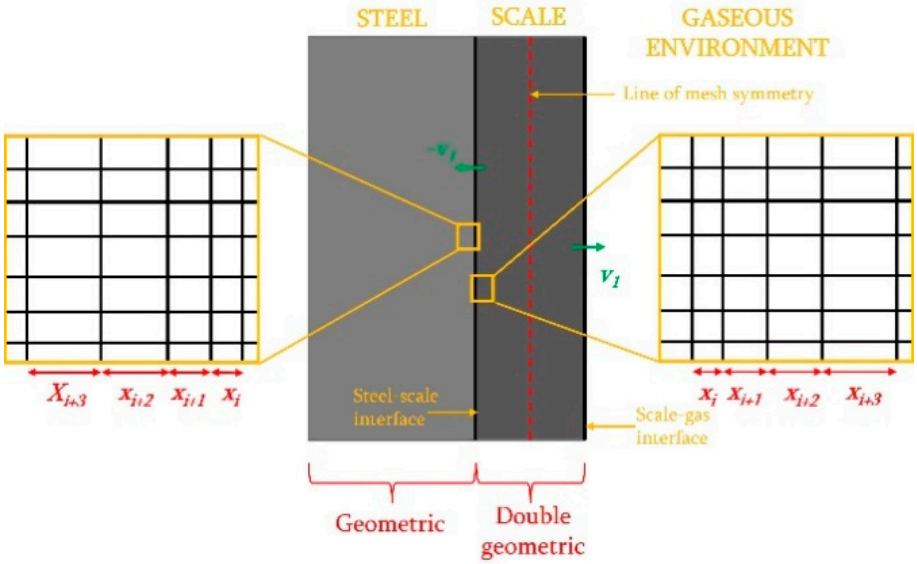

Figure 6. Geometric mesh structure for model domain.

2.2.2. Initial and Boundary Conditions

To solve the system boundary value PDE, i.e., (8), a fully implicit system was selected. Fully implicit systems carry the advantage of being unconditionally stable across all values of the mesh ratio parameter. Numerical integration was performed using the Crank–Nicolson method (see (10)).

$$-rc_{i+1}^{n+1} + (1+2r)c_i^{n+1} - rc_{i-1}^{n+1} = rc_{i+1}^{n} + (1-2r)c_i^{n} + rc_{i-1}^{n}, \text{ where } r = \frac{D\Delta t}{2(\Delta x)^2}. \quad (10)$$

The value for initial oxide thickness must be minimal but non-zero (<0.1 nm). The system is closed by assuming a 'closed' system on the metal side of the metal–gas interface, i.e., no diffusion of iron (Fe) in or out of that side of the system, and applying a fixed oxygen flux to the oxide–gas interface, corresponding to the experimental atmosphere. The combination of these conditions allows the oxide layer to grow outwards, i.e., external oxidation is assumed. To further reflect the assumption of wustite as the oxide phase, an oxygen flux of 4.5×10^{-4} $m^2 \cdot s^{-1}$ was applied by selecting the maximum value for oxygen permeability before accumulation to prevent phase transitions to magnetite and haematite,

characterised by higher oxygen content. Standard reference conditions of 298 K and 1 bar were applied for the gaseous oxygen. Both regions were discretised as a finite number of nodes (within automatically assigned meshes, as described above)

2.3. In Situ Oxidation Experiments

Complex systems where multiple reactions are anticipated, e.g., different oxide phases evolved and alternative reaction schemes are possible, are significantly influenced by sample size, form, and environment. Simultaneous Thermal Analysis (STA), a combination of Thermogravimetric Analysis (TGA) and Differential Scanning Calorimetry (DSC) uses these complementary quantitative and qualitative techniques, respectively, suitable for all solid–gas reaction studies. Wire Electrical Discharge Machining (EDM) was used to generate as geometrically consistent $3 \times 3 \times 3$ mm cubic coupons of E24 and E41 tube grade steel as possible to ensure comparable STA data. The heating action of the EDM approach introduced further oxidation to the machined coupon surfaces, which were therefore cleaned using 4000 grit polishing paper and isopropyl alcohol. Each prepared coupon was placed in the centre of an alumina crucible (which exhibits high thermal conductivity and inert behaviour towards oxygen at high temperatures). Replica heat treatment in a 10% O_2-90% N_2 atmosphere was applied sequentially to each crucible. A ramp of 5 K·s^{-1} was used for both the heating and cooling periods. Before running the thermal cycle, a 'blank' run was performed using an empty crucible to establish a buoyancy effect correction factor. Hence, uncertainty is accounted for pre-measurement. Given that the mass gain data was supplied by the STA experiment but thickness data was the output of the model, one data set required conversion. Converting the STA mass gain data demands the assumption of a fully dense oxide layer and the method itself is complexified by recognition of the fact the sample surface area is constantly changing as oxidation proceeds, i.e., sample dimensions are not fixed due to the moving steel–scale phase boundary. The alternative approach converts the model thickness data to mass gain data (see (11)).

$$\Delta m = \rho A x_1 \tag{11}$$

The value of oxide (wustite) density, ρ_{oxide}, was calculated from its molar volume, V_m, defined in the thermodynamic database, and molar mass, M_r (see (12)). The resulting value of 5914 kg·m^{-3} agreed with values found in the literature [36]. This was arguably a more accurate approach as, unlike the STA samples, within the model definition there was the existing parameter which justified the assumption of equal oxide growth across the surface, and only a single surface area, A, to consider, unlike the cubic STA samples. Ref. [11] was used to convert the model oxide thickness predictions to a total mass gain value, Δm, for the isothermal test simulated. Extension of the 1D model to 3D was achieved by extending backwards to 3 mm to match the STA samples' depth, x_1.

$$\rho_{oxide} = \frac{M_r}{V_m} \tag{12}$$

When applying the same conversion methodology to cylindrical samples, the moving phase boundary for both the SSI and SGI must be accounted for, i.e., not only is the scale layer growing radially outwards on the external surface, but the steel substrate is retreating as it is consumed during the ongoing oxidation reaction (see (13)).

$$\Delta m = \rho \pi L \left(OR^2 - (IR - \delta_{ox})^2 \right) \tag{13}$$

3. Results and Discussion

3.1. Planar Geometry

A plot of the initial validation data in the 1000 ± 1 °C for both E24 and E41 (see Figure 7) was made so that a direct comparison could be made against the identical conditions in the Thermo-Calc isothermal simulation (planar geometry heated at 1000 °C for 5 min). Figure 7

shows the comparison between the mass gain in the isothermal region of STA testing, for both grades, compared to iron oxidised in the Thermo-Calc model (converted from oxide thickness to mass gain using wustite density). Each plot is annotated with its respective parabolic rate constant.

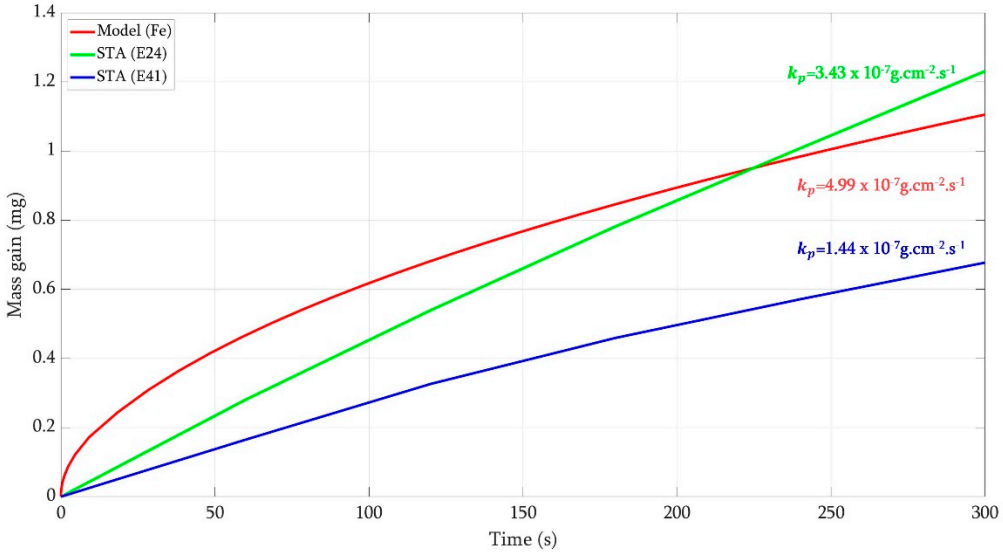

Figure 7. Comparative plot of mass gain following heating to 1000 °C for 5 min for Thermo-Calc model (red) vs. STA testing for E24 (green) and E41 (blue) tube grades, annotated with parabolic rate constant, k_p.

Although the model's predicted total mass gain lay within the range observed for the STA samples, suggesting a sufficiently accurate pre-processing methodology, its oxidation rate was higher overall. Both experimental data sets also had minimal correlation to a parabolic profile (inherent in the model due to its theoretical foundations discussed in the introduction of this work). The discrepancy between the computational and experimental results was assumed to be multi-factorial. Firstly, whilst the experimental data can be obtained directly from the equipment in a mass gain format, the model data must be converted from the thickness gain form, owing to the methodology used to make computational predictions. Whilst the experimental samples are 3 × 3 × 3 mm cubes, i.e., with six surfaces sharing the same material volume, only a single surface, i.e., 1D geometry, can be modelled, hence that single surface of equivalent area has access to six times as much material as each individual surface in the experimental samples. Hence, the mass gain associated with the model was divided by six to allow for an equivalent comparison. Furthermore, a key assumption of the model and its post-processing calculations, particularly those concerning density, was that of a perfectly compact scale layer, i.e., no porosity. However, porosity is a key property affecting diffusion mechanisms at the microstructural level. This is discussed in greater detail during geometric validation in Section 3.2, but, ultimately, it is concluded that only a modified diffusion coefficient can account for porosity and its associated effects, rather than in the pre-processing of the model [51]. In this manufacturing case, porosity was most likely to arise due to thermal deformation mismatch between the steel and scale, mechanical strength differences between phase layers (in the real case where multiple oxide phases form), the degree of vacancy annihilation (Kirkendall effect), and growth stresses due to oxidation-induced volumetric changes. Furthermore, it should be noted that Wagner's descriptive and predictive model for parabolic oxidation, which uses ionic and electronic charge transfer and balance during simultaneous metal oxidation and free oxygen reduction to characterise alloy element distribution [10], assumes a scale with a perfect microstructure and adhesion, i.e., they ignore the possibility of defects, e.g., cracks, porosity, etc., whose propagation could be accelerated by the high temperatures and mechanical work of tube stretch reduction. This is particularly important since high temperatures, such

as those used in tube normalisation, are associated with greater development of defects during cooling [18]. Such propagation has been shown to interrupt oxidation diffusion mechanisms [16], and its effect on kinetics and morphology must therefore be considered in a non-idealised approach. However, this was beyond the scope of this investigation. The STA data alone reveal a 13% difference in total mass gain between the two grades tested. This was attributed to the interactions of the dominant non-carbon alloy elements, manganese [52] and silicon [53], with iron and oxygen to form intermetallic compounds which affect oxidation kinetics and adhesion.

3.2. Cylindrical Geometry

As with the planar case, the CPU demand is low with 120 datapoints and approximately 115 s run time for each test (using a maximum timestep of 1000 s; interestingly, decreasing the maximum timestep to 100 s has no effect on the predicted oxide thickness but increases CPU demand to 899 datapoints and 684 s run time). It has been discussed that the 1D approach to diffusion modelling does not reflect the multi-axial nature of oxidation. Beyond the differences arising due to the link between geometry stress states and porosity evolution, there is also the consideration of how geometry affects diffusion pathways. The temporal concentration gradient becomes a function of $\frac{1}{r}$. Accordingly, assuming the concentration only changes due to diffusion in the radial direction, i.e., the 1D form, the radius is the discretised dimension in the numerical solution. It should be noted that, in this case, the concentration in each segment, i, is an average. When setting initial concentration conditions, $c_{i,t=0}$, and calculating average i^{th} segment concentration, every point of the circumference at radius, r, has a different weight dependent on which segment it occupies. The area of the ring with an average concentration corresponding to $c_{i,t=0}$ is defined and integration of the concentration at individual points around the ring results in an instantaneous initial average concentration. An increase in wall thickness, whilst controlling outer diameter in the same way as is carried out during tube stretch reduction and product specification, revealed a decrease in oxide thickness and the corresponding parabolic oxidation rate constants. This is due to the extension of the diffusion pathway so fewer metal cations diffuse to the SSI to react per unit time. It has also been suggested that oxidation kinetics depend on the oxide scale stress state due to the negative correlation between stress magnitude and the mole fraction of intrinsic defects within the oxide [54]. Higher stress is associated with a lower vacancy concentration, which can inhibit iron diffusion via iron vacancies. Additionally, Asensio-Jimenez et al. cited the degree of oxide growth stress relaxation by plastic deformation as a source of oxidation kinetics variation across their samples (more influential than minor alloy element depletion, which was also discussed) [55]. For example, if a sample is exposed to conditions which promote creep, the compressive and tensile stress evolved in the scale and metal, respectively, will eventually reach a level that causes substrate creep and therefore growth stress relaxation in the oxide. A thinner sample will reach this critical value sooner, i.e., have a shorter 'incubation period', and therefore initiate a period of enhanced oxidation associated with stress state changes. The difference in stress state for samples with only a small thickness difference can be significant due to the power law relationship between creep rate and the specimen thickness (although this is for flat surfaces). Although the incubation period for observing any difference in oxidation rate due to sample thickness can be far longer than is observed in the tube manufacturing process compared to a planar surface, curved surfaces will experience additional stresses associated with the forming process [56]. Asesnio-Jimenez et al. quoted as much as a 60-fold increase in substrate creep rate by decreasing specimen thickness from 0.5 to 0.3 mm. Clearly, stress cannot be directly accounted for in the thermochemical model developed; however, it should nevertheless be considered, particularly when analysing validatory data. Previous authors have investigated oxide formation on a range of tubes with varying dimensions but do not isolate a single dimension to investigate its isolated effect on oxide thickness [20,31]. This reinforces the advantages of a computational approach, as representative samples in the context of manufacturing components are often limited

to their commercial range and can be restricted at a given time to only the specifications required to meet current demand. Furthermore, the 2D diffusion pathway associated with the converging and diverging radial path of oxygen and iron ions, and the fact that their concentrations are defined normal to the surface, leads to an overlap of ion pathways, unlike in the planar case. However, the relative effect of these phenomena is dependent on the radial scale, i.e., very large radii may evolve a solution which approaches a flat plate solution as the $\frac{1}{r}$ term tends to 0. The scale at which radial effects become relevant for diffusion must be investigated. Conversely, an increase in OD, whilst controlling wall thickness, has no effect on predicted oxide thickness and parabolic rate constants. It was noted that the material was consumed approximately twice as quickly in the cylindrical case than the planar case (30 h vs. 60 h).

3.3. Radial Dependency Study

Since volume and mass gain were revealed in this work to be dependent on inner radius during oxidation, it was hypothesised that there would be a critical radius value at which the effect of cylindrical coordinates becomes influential. The effect of cylindrical geometry on the analytical theory of diffusion was outlined earlier in this work, and has been explored by other authors in an analytical context [57–60]. An initial investigation using the model explored the extremes of tube inner radial dimensions, 0.5 mm $\leq IR \leq$ 1000 mm. Volume gain, a calculation modified to reflect the cylindrical moving phase boundary and the presence of an inner, ID, and outer diameter, OD (see (13)), and its dependence on radius, was explored first and showed a strong linear relationship between volume gain and tube radius. This demonstrated that, even with the geometric conversion steps where inner radius is not involved, the physical diffusion phenomena predicted by the model are not lost, i.e., the reciprocal relation between concentration and tube radius. Further investigations were performed by exploring the relationship between mass-based parabolic rate constant (normalised against sample surface area) and tube radius (see Figure 8).

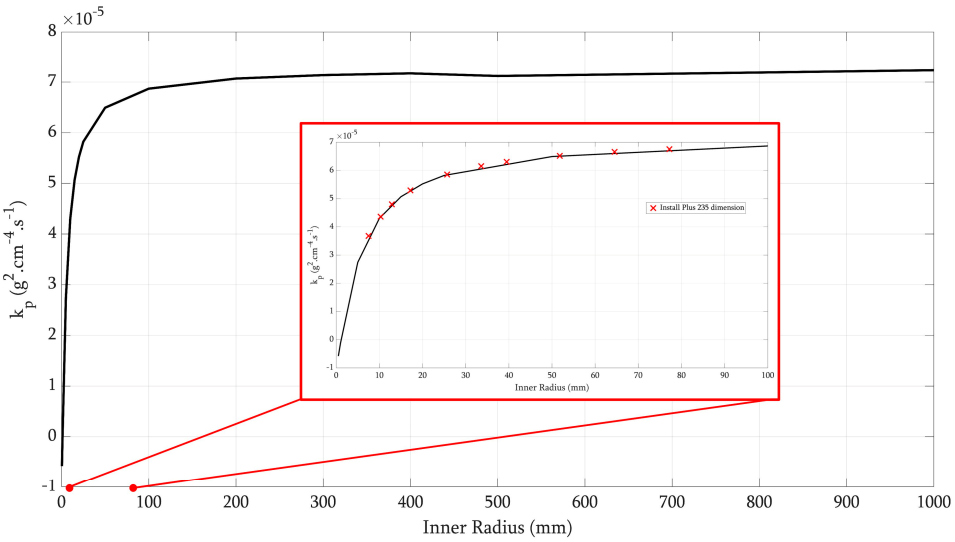

Figure 8. Plot of mass-based, surface area normalised parabolic rate constant against tube inner radius. The industrial relevant inner radius range is magnified (red box) and highlighted (red dashed line).

Crucially, the parabolic profile reveals a critical radius where radius no longer has a significant effect, associated with changes in surface area and surface area to volume ratio, as demonstrated by (2) and Figure 2, on oxidation kinetics. This change in kinetic dependency occurs at approximately 200 mm. This is an industrially relevant conclusion for typical conveyance tube applications. Furthermore, 98% of the change in thickness gain occurred in the radius range below 100 mm, again demonstrating the influence of cylindrical coordinates on conveyance tube product oxidation behaviour. This radius

region shows the sharpest change in oxidation rate. This conclusion is also supported by equivalent plots of thickness gain (see Figure 9), again suggesting a critical inner radial value of 200 mm.

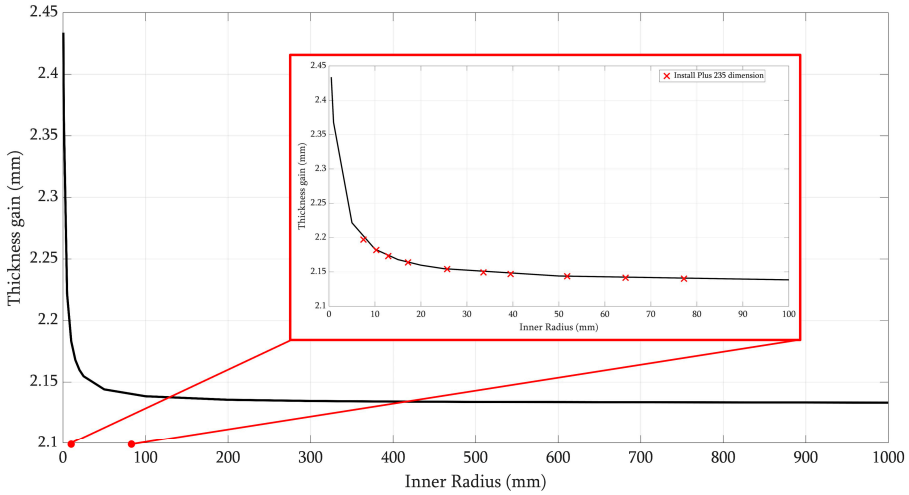

Figure 9. Plot of oxide thickness against tube inner radius. The industrial relevant inner radius range is magnified (red box) and highlighted (red dashed line).

Changes in radius are accompanied by a change in available reacting surface area and surface area to volume ratio (see Figure 2) and highlight how an increase in radius is accompanied by an increase in surface area, A, (see (3)) and a decrease in surface area to volume ratio, $A : V$ (see (4)). Therefore, the surface area increases during inner surface oxidation (consumption of the substrate widens the cylinder bore, i.e., the inner radius), which leads to an overall slower rate of reaction and therefore thinner oxide thickness after a given time and, as such, the converse is true of the outer surface.

This computational approach has enabled the extremes of potential tube dimensions to be investigated beyond that which time and sample access allows within an empirical approach. The critical radius result is industrially relevant to the range of conveyance tubes manufactured in this context, and indicates that oxidation kinetics on tubes cannot be inferred from planar components subjected to equivalent thermomechanical processing conditions. However, there are many high-temperature-application cylindrical and curved components within this dimensional range, both hollow and solid, which could benefit from the ability to understand and predict oxidation kinetics to streamline their respective manufacturing processes.

3.4. Further Work

There is little empirical data for the incorporation of porosity into the model via a modified diffusion coefficient. Porosity can influence diffusion, and subsequently oxidation, via its effect on ion migration through vacancies. The mechanically intensive processes which accompany tube manufacturing could encourage pores to propagate, amongst other defects, and capturing the effect of porosity within the model is therefore paramount to accurate oxide thickness predictions.

Attempts were made to modify the Thermo-Calc model to reflect the unavoidable heat ramp of the STA validation experiment and allow a more direct comparison. However, this came at a significant computational cost. The model complexity was also exacerbated by the introduction of a non-isothermal period due to the temperature dependence of so many of the parameters in both the thermodynamic and kinetic databases, thus introducing many more calculations to achieve a solution. The computational thermochemistry approach does not yet lend itself to efficiency over its empirical counterpart when considering non-isothermal scenarios. Hence, this work is limited to consideration of isothermal oxidation.

Although validation work was performed for the planar geometry iteration of the model using STA, the specific information surrounding curved surfaces demands its own validation using a specialist furnace to apply a representative heat treatment to tube samples.

Further techniques, such as indentation, could also be used to validate stress state analyses for both the pre- and post-normalised states.

4. Conclusions

It has been shown in this work that the undesirable, diffusion-controlled oxidation reaction, occurring on external surfaces during hot-finished conveyance tube manufacturing, and specifically the normalisation stage, can be computationally modelled. Thermo-Calc's DICTRA commercial software package can be used to solve the Stefan problem-based moving phase boundary equation for a curved surface and predict surface oxide thickness using numerical techniques, provided that bespoke thermodynamic and kinetic databases can be developed from empirical data. The following conclusions were drawn during model development:

- External surface oxide thickness on cylindrical geometries, representative of those used in conveyance applications, can be predicted quickly with ~120 datapoints.
- Dependence on the radial coordinate within the cylindrical coordinate form of the diffusion equation leads to a more complex and faster oxidation process due to continuous changes in surface area and overlapping normal diffusion pathways.
- There is a critical radius, estimated at ~200 mm, where the curvature is low enough to no longer affect oxidation, however this is still larger than the conveyance product range.

Overall, oxidation of curved surfaces appears to be more complex and unstable than its planar equivalent, a topic which has seen much greater attention in the literature. Optimal understanding and control of oxidation during conveyance tube manufacturing, and that of equivalent products, demands a separate scientific consideration.

Author Contributions: Conceptualization, M.K., H.C. and C.O.; methodology, M.K.; software, M.K.; validation, M.K.; formal analysis, M.K.; investigation, M.K.; resources, M.C., H.C., E.S., C.O. and M.A.; writing—original draft preparation, M.K.; writing—review and editing, M.C., E.S., C.O. and M.A.; visualization, E.S.; supervision, M.C., H.C., E.S., C.O. and M.A. All authors have read and agreed to the published version of the manuscript.

Funding: This research was funded by COATED M2A from the European Social Fund via the Welsh Government (c80816), the Engineering and Physical Sciences Research Council (Grant Ref: EP/S02252X/1), and Tata Steel.

Data Availability Statement: The data sets presented in this article are not readily available because this work is part of an ongoing study and is currently commercially sensitive. Requests to access the data sets should be directed to M.K.

Conflicts of Interest: M.C. was employed by the company Oxford Instruments NanoAnalysis, H.C. was employed by Frazer-Nash Consultancy, and C.O. was employed by Tata Steel. The remaining authors declare that the research was conducted in the absence of any commercial or financial relationships that could be construed as a potential conflict of interest.

References

1. Water UK. Companies Are Using New Techniques to Find and Fix More Leaks. Available online: https://www.water.org.uk/water-supply/leakage (accessed on 8 July 2024).
2. Office for National Statistics. Central Heating. Available online: https://www.ons.gov.uk/datasets/TS046/editions/2021/versions/4 (accessed on 8 July 2024).
3. Hallstrom, S.; Halvarsson, M.; Hoglund, L.; Jonsson, T.; Agren, J. High temperature oxidation of chromium: Kinetic modeling and microstructural investigation. *Solid State Ion.* **2013**, *240*, 41–50. [CrossRef]
4. Grant, J. The Development of Novel Coating Solutions for the Improvement of Pre/Post Heat Treatment Performance Properties of Carbon Steel Conveyance Tubes. Ph.D. Thesis, Department of Materials Science and Engineering, Swansea University, Swansea, Wales, UK, 2024. [CrossRef]

5. Schutze, M. The Role of Stresses in High-Temperature Corrosion: The Potential of Quantitative Approaches. *High Temp. Corros. Mater.* **2023**, *100*, 365–397. [CrossRef]
6. Matsuno, F. Blistering and Hydraulic Removal of Scale Films of Rimmed Steel at High Temperature. *Iron Steel Inst. Jpn. Int.* **1980**, *20*, 413–421. [CrossRef]
7. Birks, N.; Meier, G.H. Oxidation of Alloys. In *Introduction to High Temperature Oxidation of Metals*; Edward Arnold Ltd.: London, UK, 1983; pp. 91–130.
8. Zeng, C.; Neils, A.; Lesko, J.; Post, N. Machine learning accelerated discovery of corrosion-resistant high-entropy alloys. *Comput. Mater. Sci.* **2024**, *237*, 413–421. [CrossRef]
9. Wang, F.; Zou, D.; Wang, Q.; Zhang, X.; Tong, L.; Liang, X.; Li, Y.; Jiang, Y. The negative effect of V content on high temperature oxidation resistance of austenitic stainless steels at 850C. *Mater. Charact.* **2024**, *212*, 113967. [CrossRef]
10. Espevik, S.; Rapp, R.A.; Daniel, P.L.; Hirth, J.P. Oxidation of Ni-Cr-W Ternary Alloys. *Oxid. Met.* **1980**, *14*, 85–108. Available online: https://link.springer.com/article/10.1007/BF00603987 (accessed on 5 December 2024). [CrossRef]
11. Manning, M.I. Geometrical effects on oxide scale integrity. *Corros. Sci.* **1981**, *21*, 301–316. [CrossRef]
12. Sabau, A.S.; Wright, I.G. On the estimation of thermal strains developed during oxide growth. *J. Appl. Phys.* **2009**, *106*, 023503. [CrossRef]
13. Yu, B.; Liu, Y.; Wei, L.; Zhang, X.; Du, Y.; Wang, Y.; Ye, S. A Mechanism of Anti-Oxidation Coating Design Based on Inhibition Effect of Interface Layer on Ions Diffusion within Oxide Scale. *Coatings* **2021**, *11*, 454. [CrossRef]
14. Fu, G.Y.; Wei, L.Q.; Zhang, X.M.; Cui, Y.B.; Lv, C.C.; Ding, J.; Yu, B.; Ye, S.F. A high-silicon anti-oxidation coating for carbon steel at high temperature. *Surf. Coat. Technol.* **2017**, *310*, 166–172. [CrossRef]
15. Wu, H.; Chen, H.; Lu, J.; Feng, Y.; Zhao, S.; Guo, E. Superior anti-oxidation layer induced by PVA-boehmite sol-gel film on AISI304 steel. *Ceram. Int.* **2024**, *50*, 35273–35286. [CrossRef]
16. Pillai, R.; Chyrkin, A.; Quadakkers, W.J. Modeling in High Temperature Corrosion: A Review and Outlook. *Oxid. Met.* **2021**, *96*, 385–436. Available online: https://link.springer.com/article/10.1007/s11085-021-10033-y (accessed on 5 December 2024). [CrossRef]
17. Shajan, N.; Kumar, R.; Manik, R.; Asati, B.; Dhagde, S.; Dhangi, D.; Kumar, S.; Mahapartra, M.M.; Arora, K.S. Role of residual stress in the failure of HF-ERW welded tubes. *Eng. Fail. Anal.* **2024**, *161*, 108342. [CrossRef]
18. Soori, M.; Arezoo, B. A Review in Machining-Induced Residual Stress. *J. New Technol. Mater.* **2022**, *12*, 64–83. Available online: https://hal.science/hal-03679993v1 (accessed on 5 December 2024).
19. Wang, C.; Wu, H.; Zhang, P.; Li, Z.; Cao, R.; Shang, C. Analysis of the Local Plastic Deformation of the Surface Oxide Layer formed on Low-Alloy High-strength Steel. *Trans. Indian Inst. Met.* **2022**, *75*, 1441–1450. [CrossRef]
20. Wassilkowska, A.; Wojciech, D. Silicon as a component of ferric oxide scale covering ductile iron pipes after annealing. *Eng. Fail. Anal.* **2021**, *125*, 105381. [CrossRef]
21. Picque, B.; Bouchard, P.-O.; Montmitonnet, P.; Picard, M. Mechanical behaviour of iron oxide scale: Experimental and numerical study. *Wear* **2006**, *260*, 231–242. [CrossRef]
22. Sun, L.; Yan, W. Estimation of Oxidation Kinetics and Oxide Scale Void Position of Ferritic-Martensitic Steels in Supercritical Water. *Adv. Mater. Sci. Eng.* **2017**, *2017*, 9154934. [CrossRef]
23. Spencer, P.J. A brief history of CALPHAD. *Comput. Coupling Phase Diagr. Thermochem.* **2008**, *32*, 1–8. [CrossRef]
24. Hillert, M. The compound energy formalism. *J. Alloys Compd.* **2001**, *320*, 161–176. [CrossRef]
25. Poerschke, D.L. Developments in Thermodynamic Models of Deposit-Induced Corrosion of High-Temperature Coatings. *J. Miner. Met. Mater. Soc.* **2022**, *24*, 260–273. [CrossRef]
26. Thermo-Calc Software AB. Diffusion Module (DICTRA) Documentation Set. ed, 2023, pp. 23–34. Available online: https://thermocalc.com/support/documentation/ (accessed on 7 August 2023).
27. Wilkstrom, P.; Blasiak, W.; Du, S.C. A study on oxide scale formation of low carbon steel using thermo gravimetric technique. *Ironmak. Steelmak.* **2008**, *35*, 621–632. [CrossRef]
28. Lee, J.H.; Noh, W.; Kim, D.; Lee, M. Spallation analysis of oxide scale on low carbon steel. *Mater. Sci. Eng. A* **2016**, *676*, 385–394. [CrossRef]
29. Basabe, V.; Szpunar, J. Phase Composition of Oxide Scales during Reheating in Hot Rolling of Low Carbon Steel. *Steel Res. Int.* **2006**, *27*, 818–824. Available online: https://onlinelibrary.wiley.com/doi/epdf/10.1002/srin.200606467 (accessed on 5 December 2024). [CrossRef]
30. Landfahrer, M.; Schluckner, C.; Prieler, R.; Gerhardter, H.; Zmek, T.; Klarner, J.; Hochenauer, C. Numerical and experimental investigation of scale formation on steel tubes in a real-size reheating furnace. *Int. J. Heat Mass Transf.* **2019**, *129*, 460–467. [CrossRef]
31. Purbolaksono, J.; Khinani, A.; Rashid, A.Z.; Ali, A.A.; Nordin, N.F. Prediction of oxide scale growth in superheater and reheater tubes. *Corros. Sci.* **2009**, *51*, 1022–1029. [CrossRef]
32. Sun, L.; Yan, W. Prediction of wall temperature and oxide scale thickness of ferritic–martensitic steel superheater tubes. *Appl. Therm. Eng.* **2018**, *134*, 171–181. [CrossRef]

33. Hsueh, C.H.; Evans, A.G. Oxidation induced stresses and some effects on the behavior of oxide films. *J. Appl. Phys.* **1983**, *54*, 6672–6686. [CrossRef]
34. Iordanova, I.; Surtchev, M.; Forcey, K.S.; Krastev, V. High-temperature surface oxidation oflow-carbon rimming steel. *Surf. Interface Anal.* **2000**, *30*, 158–160. [CrossRef]
35. Jang, J.H.; Lee, D.E.; Kim, M.Y.; Kim, H.G. Investigation of the slab heating characteristics in a reheating furnace with the formation and growth of scale on the slab surface. *Int. J. Heat Mass Transf.* **2010**, *53*, 4326–4332. [CrossRef]
36. Chen, R.Y.; Yeun, W.Y.D. Review of the High-Temperature Oxidation of Iron and Carbon Steels in Air or Oxygen. *Oxid. Met.* **2003**, *59*, 433–468. Available online: https://link.springer.com/article/10.1023/A:1023685905159 (accessed on 5 December 2024). [CrossRef]
37. Birks, N.; Meier, G.H. Mechanisms of Oxidation. In *Introduction to High Temperature Oxidation of Metals*; Edward Arnold Ltd.: London, UK, 1983; pp. 31–65.
38. Hidayat, T.; Shishin, D.; Jak, E.; Decterov, S.A. Thermodynamic reevaluation of the Fe–O system. *Calphad* **2015**, *48*, 131–144. [CrossRef]
39. Sundman, B. An Assessment of the Fe-O system. *J. Phase Equilibria* **1991**, *12*, 127–140. Available online: https://link.springer.com/article/10.1007/BF02645709 (accessed on 5 December 2024). [CrossRef]
40. Hallstrom, S.; Hoglund, L.; Agren, J. Modeling of iron diffusion in the iron oxides magnetite and hematite with variable stoichiometry. *Acta Mater.* **2010**, *59*, 53–60. [CrossRef]
41. Xia, C.; Xia, S.; Li, Y.; Lu, X. Evaluating atomic mobility and interdiffusivity based on two-dimensional diffusion simulations and diffusion triple experiments. *Scr. Mater.* **2020**, *188*, 124–129. [CrossRef]
42. Koga, S.; Krstic, M. Phase Change Model: Stefan Problem. In *Materials Phase Change PDE Control & Estimation*; Birkhäuser: Cham, Switzerland, 2020; pp. 1–13. [CrossRef]
43. Larsson, H. A model for 1D multiphase moving phase boundary simulations under local equilibrium conditions. *Calphad* **2014**, *47*, 1–8. [CrossRef]
44. Welded Steel Tubes for Pressure Purposes—Technical Delivery Conditions (Part 2: Electric Welded Non-Alloy and Alloy Steel Tubes with Specified Elevated Temperature Properties), BS EN10217-2, 2019. [Online]. Available online: https://bsol.bsigroup.com/Bibliographic/BibliographicInfoData/000000000030438140 (accessed on 5 December 2024).
45. Kowalski, M.; Spencer, P.J. Thermodynamic reevaluation of the C-O, Fe-O and Ni-O systems: Remodelling of the liquid, BCC and FCC phases. *Calphad* **1995**, *19*, 229–243. [CrossRef]
46. Hazen, R.M.; Jeanloz, R. Wüstite (Fe1-x O): A review of its defect structure and physical properties. *Rev. Geophys.* **1984**, *22*, 37–46. [CrossRef]
47. Thermo-Calc Software AB. Database Manager User Guide. In *Thermo-Calc Documentation Set*; Thermo-Calc Software AB: Solna, Sweden, 2023; pp. 1743–1840. Available online: https://thermocalc.com/support/documentation/ (accessed on 5 December 2024).
48. Gamsjager, E.; Svoboda, J.; Fischer, F.D. Austenite-to-ferrite phase transformation in low-alloyed steels. *Comput. Mater. Sci.* **2005**, *32*, 360–369. [CrossRef]
49. Bornstein, L. *Numerical Data and Functional Relationships in Science and Technology: Group III*; Springer: Berlin/Heidelberg, Germany, 1990; Volume 26.
50. Kofstad, P. Oxides of Group VII and VIII Elements. In *Nonstoichiometry, Diffusion, and Electrical Conductivity in Binary Oxides*; John Wiley & Sons: London, UK, 1972; pp. 213–264.
51. Imbrie, P.K.; Lagoudas, D.C. Morphological Evolution of TiO2 Scale Formed on Various 1D and 2D Geometries of Titanium. *Oxid. Met.* **2001**, *55*, 359–399. Available online: https://link.springer.com/article/10.1023/A:1010368412822 (accessed on 5 December 2024). [CrossRef]
52. Aghaeian, S.; Sloof, W.G.; Mol, J.M.C.; Bottger, A.J. Initial High-Temperature Oxidation Behavior of Fe–Mn Binaries in Air: The Kinetics and Mechanism of Oxidation. *Oxid. Met.* **2022**, *98*, 217–237. [CrossRef]
53. Birosca, S.; Dingley, D.; Higginson, R.L. Microstructural and microtextural characterization of oxide scale on steel using electron backscatter diffraction. *J. Microsc.* **2004**, *213*, 235–240. [CrossRef] [PubMed]
54. Simon, D.; Gorr, B.; Christ, H.J. Effect of Atmosphere and Sample Thickness on Kinetics, Microstructure, and Compressive Stresses of Chromia Scale Grown on Ni–25Cr. *Oxid. Met.* **2017**, *87*, 417–429. [CrossRef]
55. Asensio-Jimenez, C.; Niewolak, L.; Hattendorf, H.; Kuhn, B.; Huczkowski, P.; Singheiser, L.; Quadakkers, W.J. Effect of Specimen Thickness on the Oxidation Rate of High Chromium Ferritic Steels: The Significance of Intrinsic Alloy Creep Strength. *Oxid. Met.* **2012**, *79*, 15–28. [CrossRef]
56. Nygren, K.E.; Yu, Z.; Rouillard, F.; Couet, A. Effect of sample thickness on the oxidation and carburization kinetics of 9Cr-1Mo steel in high and atmospheric pressure CO_2 at 550 °C. *Corros. Sci.* **2020**, *163*, 108292. [CrossRef]
57. Auinger, M.; Buchler, M.; Schoneich, H.; Gierl-Mayer, C.; Danninger, H. Hydrogen accumulation and diffusion in cylindrical-shaped pipeline steels with coating defects. *Int. J. Hydrogen Energy* **2023**, *48*, 34454–34462. [CrossRef]
58. Degasperi, A.; Calder, M. Relating PDEs in Cylindrical Coordinates and CTMCs with Levels of Concentration. *Electron. Notes Theor. Comput. Sci.* **2010**, *268*, 49–59. [CrossRef]

59. Entchev, P.B.; Lagoudas, D.C.; Slattery, J.C. Effects of non-planar geometries and volumetric expansion in the modeling of oxidation in titanium. *Int. J. Eng. Sci.* **2001**, *39*, 695–714. [CrossRef]
60. Wang, P.; Du, K.; Yin, H.; Wang, D. Enhancing oxide scale growth and adhesion via electrochemically regulating ion diffusion. *J. Mater. Sci. Technol.* **2023**, *158*, 133–144. [CrossRef]